Eur. Phys. J. C (2026) 86:17
https://doi.org/10.1140/epjc/s10052-025-15245-z

THE EUROPEAN PHYSICAL JOURNAL C

Regular Article - Theoretical Physics

Quasinormal modes and greybody factors of black holes corrected by nonlinear electrodynamics

Jie Liang[1], **Dong Liu**[2], **Zheng-Wen Long**[1,a]

[1] College of Physics, Guizhou University, Guiyang 550025, China
[2] Department of Physics, Guizhou Minzu University, Guiyang 550025, China

Received: 17 April 2025 / Accepted: 22 December 2025
© The Author(s) 2026

Abstract Can models that are degenerate in electromagnetic observations (i.e., having identical shadows) be distinguished by their dynamical behaviors and quantum radiation properties? To address this question, this paper considers a unique charged black hole with logarithmic term corrections in NED (Mazharimousavi in Phys Lett B 841:137948, 2023, https://doi.org/10.1016/j.physletb.2023.137948, arXiv:2305.01048 [gr-qc]). It is found that for models degenerate with the shadow of a Schwarzschild black hole, although the oscillation frequencies (real parts) of their quasinormal modes (QNMs) are almost indistinguishable, their decay rates (imaginary parts) exhibit significant sensitivity. This provides the primary criterion for breaking the observational degeneracy. Furthermore, to investigate the effect of parameters, it is observed that when the parameter ζ is fixed, the deviation behavior of QNM frequencies from those of the Schwarzschild black hole follows a more distinct pattern: the oscillation frequency decreases almost linearly with the increase in charge q, while the decay rate shows a stronger nonlinear dependence. In addition, the analysis of greybody factors (GFs) offers a second approach for distinction. It reveals a more complex non-monotonic behavior: in the low-frequency region, the transmittance of the Schwarzschild black hole is higher; however, above a cross frequency, the transmittance of the NED model rapidly surpasses that of the former. These results indicate that the damping time of QNMs and the precise shape of the Hawking radiation spectrum, rather than the shadow size, are more sensitive physical observables for detecting such logarithmic corrections. This study provides specific and distinguishable theoretical criteria for testing and constraining such NED models using gravitational wave astronomy and high-precision radiation observations in the future.

1 Introduction

In recent years, black hole research has advanced from theoretical prediction to observational verification. The detection of gravitational wave signals generated by binary black hole mergers by the LIGO-Virgo-KAGRA collaboration [2–5], along with the imaging of the shadow of the supermassive black hole at the center of M87* by the Event Horizon Telescope (EHT) [6], not only provides direct evidence for the existence of black holes but also opens unprecedented opportunities for the precise testing of general relativity (GR) and the exploration of new physics beyond the standard model in strong gravitational fields [7,8].

However, although the black hole shadow observed by the EHT is highly consistent with the predictions of GR, it cannot completely rule out alternative gravitational or matter field theories that can produce identical shadows. This observation has potential degeneracy, creating an urgent need for independent probes capable of detecting deeper dynamical properties of black hole spacetimes. For this purpose, QNMs offer an ideal approach. As the dominant damped oscillations in the late-time response of a black hole to external perturbations, their properties are jointly determined by the characteristics of the background spacetime and the perturbation field. The complex frequency spectrum of QNMs not only encodes information about the black hole's mass, angular momentum, and charge but also contains features of any possible deviations from GR caused by quantum corrections or modified gravitational theories [9–12]. Thus, the precise determination of QNMs has become a cornerstone for testing the black hole no-hair theorem and gravitational theories [13–18]. In addition, GFs constitute another independent quantum probe for detecting spacetime geometry. They are directly related to the final shape of the observable Hawking radiation spectrum and have a corresponding rela-

[a] e-mail: zwlong@gzu.edu.cn (corresponding author)

Published online: 12 January 2026

tionship with QNMs in the geometric optics limit [19–21]. Due to the high sensitivity of GFs to black hole geometry, gravity, and matter theories, their analysis provides a complementary approach for identifying physical signals beyond the standard Einstein–Maxwell theory [22–26].

Among the numerous explorations beyond the standard Einstein–Maxwell theory, the coupling of GR with NED represents a fruitful research direction. Its initial motivation was to resolve the self-energy divergence problem of point charges [27], and it can naturally yield regular black hole solutions [27–32]. Extensive studies on the observable characteristics of various NED black holes aim to provide clues for distinguishing between different gravitational or matter field theories [33–39]. Against this background, this paper focuses on a unique NED black hole model recently proposed by Mazharimousavi et al. [1]. The motivation for this model is to phenomenologically simulate quark-like confinement potentials in particle physics, leading to a spacetime metric that includes a core logarithmic correction term in addition to the standard Reissner–Nordström (R–N) terms. This unique physical origin naturally gives rise to the core question of this paper: Can such logarithmic corrections, derived from confinement-like potentials, leave identifiable and unique "fingerprints" in the QNMs and GFs of black holes, thereby breaking the model degeneracy existing in electromagnetic observations?

The structure of this paper is arranged as follows: Sect. 2 introduces the spacetime metric of the logarithmically corrected NED black hole model and incorporates the observational constraints from M87*. Section 3 discusses the perturbation equations of the scalar field in this spacetime. Sections 4 and 5 present the calculation method and numerical results of QNMs. Section 6 analyzes the greybody factors. Section 7 provides a summary of the entire paper. Finally, there is an Appendix A. In this paper, we adopt the geometric unit system ($c = G = 1$).

2 NED-corrected black hole spacetime

We consider a system where Einstein gravity is minimally coupled to an NED model with quark-like confinement properties. The total action of the system is given by [1]:

$$S = \int d^4x\sqrt{-g}\left[\frac{\mathcal{R}}{16\pi G} + \mathcal{L}\right], \tag{1}$$

where $\mathcal{R}$ denotes the Ricci scalar, g is the metric determinant, and G is the gravitational constant. The Lagrangian density of the matter sector, $\mathcal{L}_{\mathcal{F}} = \frac{1}{4}F_{\mu\nu}F^{\mu\nu}$, is a nonlinear function of the Maxwell invariant, with its specific form expressed as:

$$\mathcal{L} = -\frac{16\left(3\sqrt{-2\mathcal{F}} + \zeta\left(\zeta + \sqrt{\zeta^2 + 4\sqrt{-2\mathcal{F}}}\right)\right)\sqrt{-2\mathcal{F}}}{3\left(\zeta + \sqrt{\zeta^2 + 4\sqrt{-2\mathcal{F}}}\right)^4}\mathcal{F}. \tag{2}$$

In the equation above, ζ is the nonlinear coupling parameter. By varying the action, the dynamical equations of the system are derived. The gravitational field equation is:

$$G^{\nu}_{\mu} = 8\pi T^{\nu}_{\mu}, \tag{3}$$

Here, G^{ν}_{μ} is the Einstein tensor, and T^{ν}_{μ} represents the energy-momentum tensor, whose expression is:

$$T^{\nu}_{\mu} = \frac{1}{4\pi}\left(\mathcal{L}\delta^{\nu}_{\mu} - \mathcal{L}_{\mathcal{F}}F_{\mu\lambda}F^{\nu\lambda}\right), \tag{4}$$

where $\mathcal{L}_F = \frac{\partial\mathcal{L}}{\partial F}$ (the partial derivative of the Lagrangian density with respect to the Maxwell invariant $\mathcal{F}$), δ^{ν}_{μ} is the Kronecker delta, and $F_{\mu\lambda}$ is the electromagnetic field tensor.

Assuming spherical symmetry, the line element is expressed as:

$$ds^2 = -f(r)dt^2 + \frac{dr^2}{f(r)} + r^2(d\theta^2 + \sin^2\theta d\phi^2). \tag{5}$$

Substituting this metric into the Einstein-NED coupled field Eq. (3) and solving it, the metric function describing the black hole spacetime can be obtained:

$$f(r) = 1 - \frac{2M}{r} + \frac{q^2}{r^2} - \frac{4q\sqrt{q}\zeta}{3r}\ln(r), \tag{6}$$

where M and q are the mass and charge of the black hole, respectively. When the nonlinear coupling parameter $\zeta = 0$, this metric reduces to the standard R–N solution; when the charge $q = 0$, it further reduces to the Schwarzschild black hole. The last term in Eq. (6) – which contains a logarithmic term-characterizes the coupling effect between the nonlinear electromagnetic field and gravity. As noted in Reference [1], the slow-decay property of this logarithmic term generates an effective long-range confinement-like force. This force acts on test particles at large distances and can alleviate anomalies in their velocity-radius curves.

To make physically reasonable predictions for the QNMs of this model, it is necessary to first determine the astrophysically allowed range of its parameters (q, ζ). Therefore, the core task of this section is to impose constraints on the parameter space of this NED-corrected black hole model using observational data of the supermassive black hole M87* from the EHT. For this purpose, we will first systematically analyze the horizon structure of the model, then calculate the black hole shadow size, and compare the theoretical predictions with the EHT observational results.

The horizon structure of the spacetime is determined by the roots of the metric function $f(r) = 0$, and its properties depend on the extremum of $f(r)$ at its extreme point r_c. The point r_c is determined by $f'(r) = 0$, where the expression for $f'(r)$ is:

$$f'(r) = \frac{2M}{r^2} - \frac{2q^2}{r^3} - \frac{4q\sqrt{q}\zeta}{3r^2}\left(1 - \ln(r)\right). \tag{7}$$

At the critical point $r = r_c$, let $f'(r_c) = 0$, thereby obtaining an implicit equation defining r_c. Although we cannot analytically solve for r_c, we can use this condition to simplify the expression for $f(r_c)$. From $f'(r_c) = 0$, we have:

$$\frac{2M}{r_c} = \frac{2q^2}{r_c^2} + \frac{4q\sqrt{q}\zeta}{3r_c}\left(1 - \ln(r_c)\right). \tag{8}$$

Substituting Eq. (8) into the expression for $r = r_c$ in Eq. (6), the term $2M/r_c$ can be eliminated:

$$\begin{aligned} f(r_c) &= 1 - \left[\frac{2q^2}{r_c^2} + \frac{4q\sqrt{q}\zeta}{3r_c}\left(1 - \ln(r_c)\right)\right] \\ &\quad + \frac{q^2}{r_c^2} - \frac{4q\sqrt{q}\zeta}{3r_c}\ln(r_c) \\ &= 1 - \frac{q^2}{r_c^2} - \frac{4q\sqrt{q}\zeta}{3r_c}. \end{aligned}$$

At the extreme point r_c of the metric function $f(r)$, its function value $f(r_c)$ directly determines the number of real roots of the equation $f(r) = 0$. Specifically: $f(r_c) \leq 0$ corresponds to two roots, $f(r_c) = 0$ corresponds to one root (the extreme point is the root), and $f(r_c) \geq 0$ corresponds to no real roots. Based on this, we define an effective discriminant $\Delta_{\text{eff}} \equiv f(r_c)$, whose value is implicitly determined by the model parameters (q, ζ) through r_c:

$$\Delta_{\text{eff}}(q, \zeta) = 1 - \frac{A}{r_c} - \frac{q^2}{r_c^2}, \tag{9}$$

where $A = (4/3)q\sqrt{q}\zeta$. The sign of this discriminant determines the structure of the black hole horizon: $\Delta_{\text{eff}} < 0$ indicates the spacetime has two inner and outer horizons (non-extremal black hole); $\Delta_{\text{eff}} = 0$ corresponds to an extremal black hole with a single horizon; and $\Delta_{\text{eff}} > 0$ corresponds to a naked singularity without a horizon. Figure 1(a) exemplifies the behavior of the metric function in these three cases, corresponding to $f(r) = 0$ having two(blue solid line), one(red dashed line), or zero positive real roots(green dashed line), respectively. Figure 1(b) intuitively shows the horizon structure regions divided by the sign of the discriminant in the parameter space (q, ζ), providing a basis for understanding the theoretical completeness of the model.

We regard this NED-corrected black hole model as a candidate theory for the central object of M87* and use EHT observational data to impose constraints on its parameters.

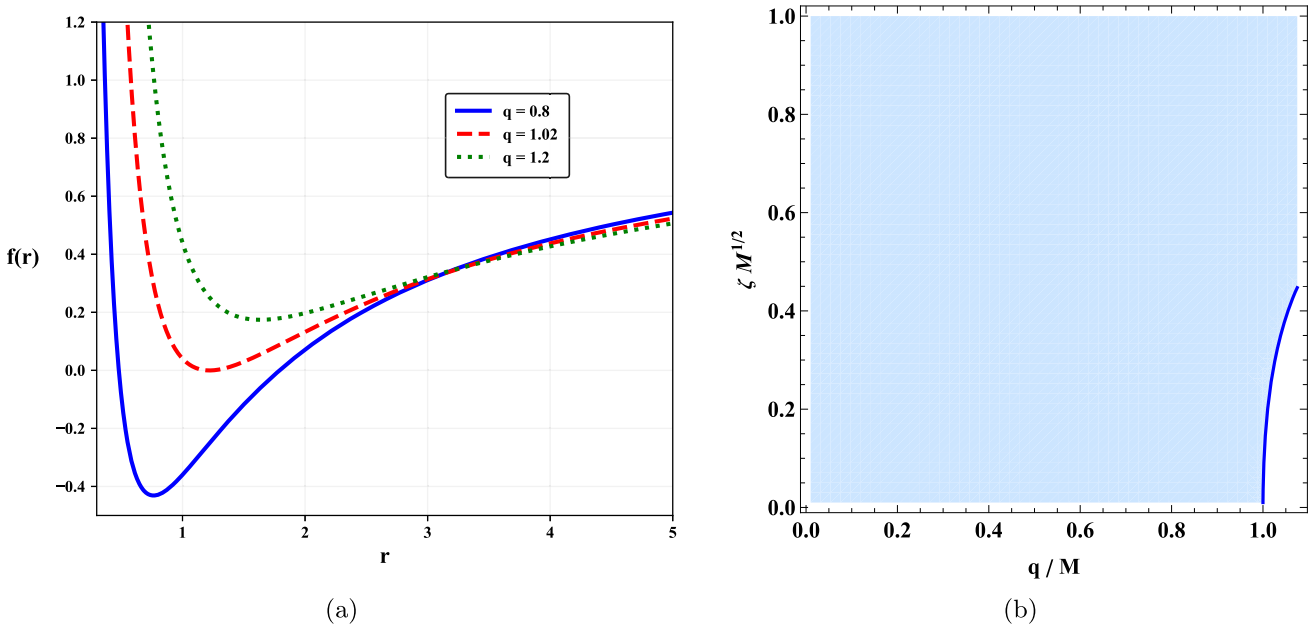

Fig. 1 (**a**) Variation of the metric function $f(r)$ with the radial coordinate r. This figure fixes $\zeta = 0.268$ and shows the influence of different charge parameters q on the metric function. (**b**) Black hole horizon structure in the parameter space (q, ζ). The light blue region corresponds to non-extremal black holes with inner and outer double horizons; the white region corresponds to naked singularities; the blue boundary line represents extremal black holes. The parameters in the figure are set to $M = 1$.

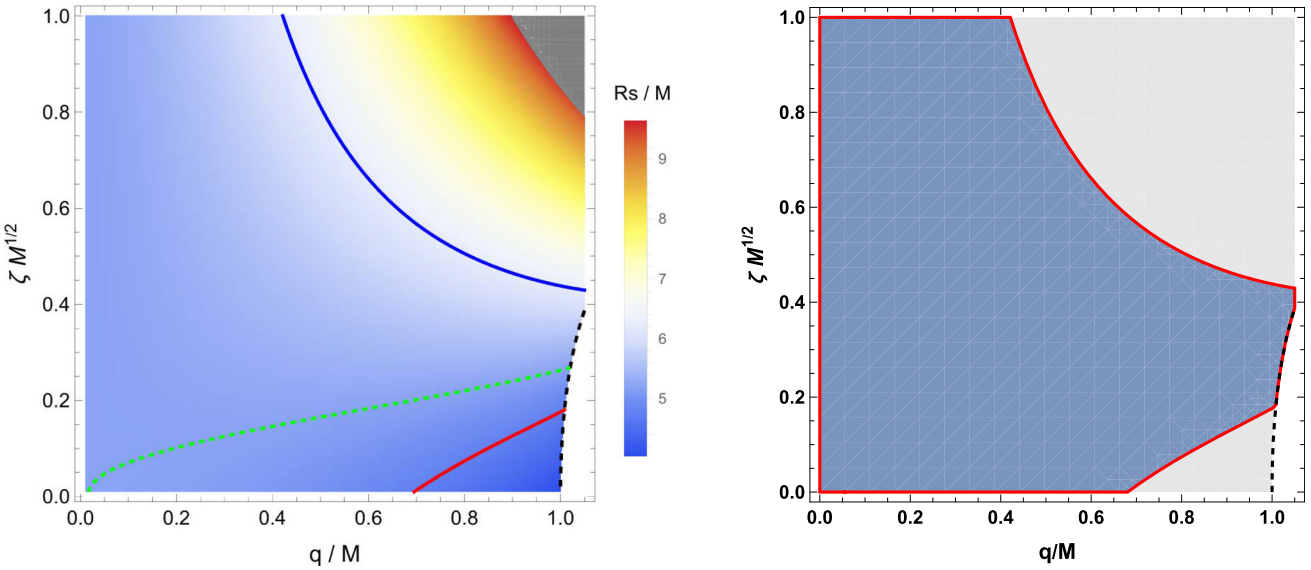

Fig. 2 Theoretical analysis of the NED-corrected black hole and observational constraints from M87*. (**a**) Theoretical predicted distribution of the ratio of black hole shadow radius to mass R_s/M in the parameter space. The contour lines in the figure show how R_s/M depends on the model parameters. (**b**) Final physical constraint results. The blue shaded region in the figure shows the parameter range where the theoretically predicted shadow size is consistent with the EHT observation of M87* at the 1σ confidence level

Light from distant celestial bodies is deflected in the strong gravitational field of the black hole, and some of the photons are captured by the gravitational field and orbit on specific unstable circular orbits, thereby forming a photon sphere. For a static spherically symmetric spacetime, the photon sphere radius $r_{\rm ps}$ can be determined by the following formula [40]:

$$r_{\rm ps} f'(r_{\rm ps}) - 2 f(r_{\rm ps}) = 0. \tag{10}$$

For a static observer at a great distance, the radius $R_{\rm s}$ of the black hole shadow can be accurately calculated from the photon sphere radius and the spacetime geometry at its location [41,42]:

$$R_{\rm s} = \frac{r_{\rm ps}}{\sqrt{f(r_{\rm ps})}}. \tag{11}$$

Since this paper studies a static spherically symmetric spacetime, the black hole shadow it produces is a perfect circle geometrically. Therefore, the model parameters (ζ, q) only affect the radius $R_{\rm s}$ of the shadow by changing the function $f(r)$, without altering its circular geometric structure. In this NED-corrected model, the parameters (q, ζ) directly affect the position of the photon sphere and the shadow radius by changing the metric function $f(r)$. Compared with the fixed shadow radius of the Schwarzschild black hole ($q = 0, \zeta = 0$), $R_{\rm s}^{\rm Sch} = 3\sqrt{3}M \approx 5.196M$, the shadow size predicted by this model can vary within a certain range. To quantify this behavior, we systematically calculated the theoretical distribution of $R_{\rm s}/M$ in the entire parameter space by numerically solving Eqs. (10) and (11), and the results are shown in Fig. 2a. This map establishes a direct mapping from model parameters to observable quantities and reveals the core feature of the shadow radius: As illustrated by the color gradient, if either ζ or q remains in the low-value range, the variation of R_s is relatively gentle, confined mostly to the blue to light-blue regions. Conversely, when both parameters lie in the high-value range (top-right corner), the shadow radius exhibits a sharp increasing trend. This phenomenon indicates a synergistic effect between q and ζ: a high ζ value significantly enhances the spacetime distortion induced by the charge, resulting in a substantial enlargement of the observed shadow.

To constrain the model parameters, we compare the theoretical predictions with the EHT observational results of M87*. According to the EHT release, the angular diameter of the shadow of M87* is $42 \pm 3\,\mu$as [6], corresponding to an angular radius $\theta_{\rm s} = 21 \pm 1.5\,\mu$as. Combined with the independently measured black hole mass $M = (6.5 \pm 0.7) \times 10^9 M_\odot$ and distance $D = 16.8 \pm 0.8\,$Mpc [6], the physical radius and angular radius of the shadow are related by $R_{\rm s} = \theta_{\rm s} \cdot D$. Thus, the ratio of the shadow radius to the mass is:

$$\frac{R_{\rm s}}{M} = \frac{\theta_{\rm s} \cdot D}{M}. \tag{12}$$

Based on the standard error propagation theory and assuming that the uncertainties of each observable are independent of each other, the relative uncertainty of $R_{\rm s}/M$ is obtained as:

Table 1 Parameters of the NED-corrected black hole with the same shadow radius as the Schwarzschild black hole

Parameter	Schwarzschild	Dual-horizon black hole				Extremal black hole
q/M	0.0	0.2	0.4	0.6	0.8	1.02
$\zeta M^{1/2}$	0.00	0.102	0.146	0.183	0.220	0.268

$$\frac{\delta(R_s/M)}{R_s/M} = \sqrt{\left(\frac{\delta\theta_s}{\theta_s}\right)^2 + \left(\frac{\delta D}{D}\right)^2 + \left(\frac{\delta M}{M}\right)^2}, \tag{13}$$

It is calculated that the observed value of R_s/M is [4.75, 6.25] within the 1σ confidence interval.

We plot the 1σ observational confidence interval determined by Eq. 13 together with the theoretical predictions in the parameter space diagram (Fig. 2a), thereby selecting the parameter region compatible with the observational results at the 1σ confidence level. In the figure, the red and blue solid lines respectively delimit the constraint ranges determined by the upper and lower limits of the observed angular radius R_s/M ($R_s/M = 4.75$ and $R_s/M = 6.25$). For reference, the green dashed line marks the parameter combinations equal to the shadow radius of the Schwarzschild black hole ($R_s/M \approx 5.196$). The specific values are listed in Table 1. The gray region in the upper right corner of the figure represents the case of a naked singularity (i.e., $f(r_c) > 0$), so the corresponding parameter combinations should be excluded physically. Finally, Fig. 2b clearly shows the parameter region (blue shaded area) that satisfies the 1σ observational constraints. This indicates that the NED-corrected black hole model can be compatible with the current highest-precision black hole shadow observational data within this parameter range.

When analyzing the degeneracy, we deliberately included a complete parameter sequence from non-extremal black holes to the boundary of extremal black holes. In particular, the parameter combination ($q/M = 1.02, \zeta M^{1/2} = 0.268$) listed in Table 1 corresponds to the boundary case of an extremal black hole ($\Delta_{\text{eff}} = 0$). It is important to emphasize that although we incorporated this extremal case into the degeneracy analysis to explore the full theoretical possibilities, our main physical analyses (including M87* observational constraints and QNM calculations) are strictly restricted to the parameter region of non-extremal black holes. The blue shaded area in Fig. 2b lies entirely within the non-extremal black hole region, while the extremal black hole point serves only as a reference for the theoretical boundary. This approach allows us to comprehensively evaluate the scope of model degeneracy while ensuring that all physical conclusions are based on black hole models with a complete horizon structure.

3 Scalar field perturbations

Considering the spacetime background described by the metric (6), we study the perturbation behavior of a massless test scalar field Φ. The dynamical behavior of this field is governed by the Klein–Gordon (K–G) equation, whose specific form in curved spacetime is:

$$\frac{1}{\sqrt{-g}}\partial_\mu\left(\sqrt{-g}g^{\mu\nu}\partial_\nu\Phi\right) = 0. \tag{14}$$

Substituting the separation of variables form $\Phi(t, r, \theta, \phi) = \frac{1}{r}\Psi(t, r)Y_{lm}(\theta, \phi)$ into the covariant K–G equation (14), the angular part can be separated out via the eigenvalue $-l(l+1)$ of the spherical harmonic function. The radial part is expressed as:

$$-\frac{1}{f(r)}\frac{\partial^2\Psi}{\partial t^2} + \frac{\partial}{\partial r}\left(f(r)\frac{\partial\Psi}{\partial r}\right) - \frac{l(l+1)f(r)}{r^2}\Psi = 0. \tag{15}$$

By introducing the tortoise coordinate $dr_* = \frac{dr}{f(r)}$, the radial wave Eq. (15) can be transformed into a Schrödinger-like equation:

$$\frac{\partial^2\Psi}{\partial t^2} - \frac{\partial^2\Psi}{\partial r_*^2} + V_{\text{eff}}(r)\Psi = 0, \tag{16}$$

where the effective potential is written as:

$$V_{\text{eff}}(r) = f(r)\left(\frac{l(l+1)}{r^2} + \frac{1}{r}\frac{df(r)}{dr}\right). \tag{17}$$

To further explore how model parameters affect the spacetime structure around the black hole, we analyzed the characteristic behavior of the effective potential V_{eff} for scalar field perturbations, as shown in Fig. 3.

In figure (a), we compare the Schwarzschild black hole with the NED-corrected black hole that have the same shadow radius. The results show that the latter exhibits a lower potential barrier peak and a wider barrier shape, and this trend becomes more significant as the parameters q and ζ increase.

In figure (b), the increase in the angular quantum number l significantly raises the peak value $V_{\max}$ of the potential barrier. This phenomenon is consistent with physical expectations, because the contribution of the centrifugal potential term $f(r)\frac{l(l+1)}{r^2}$ in the effective potential increases with l and

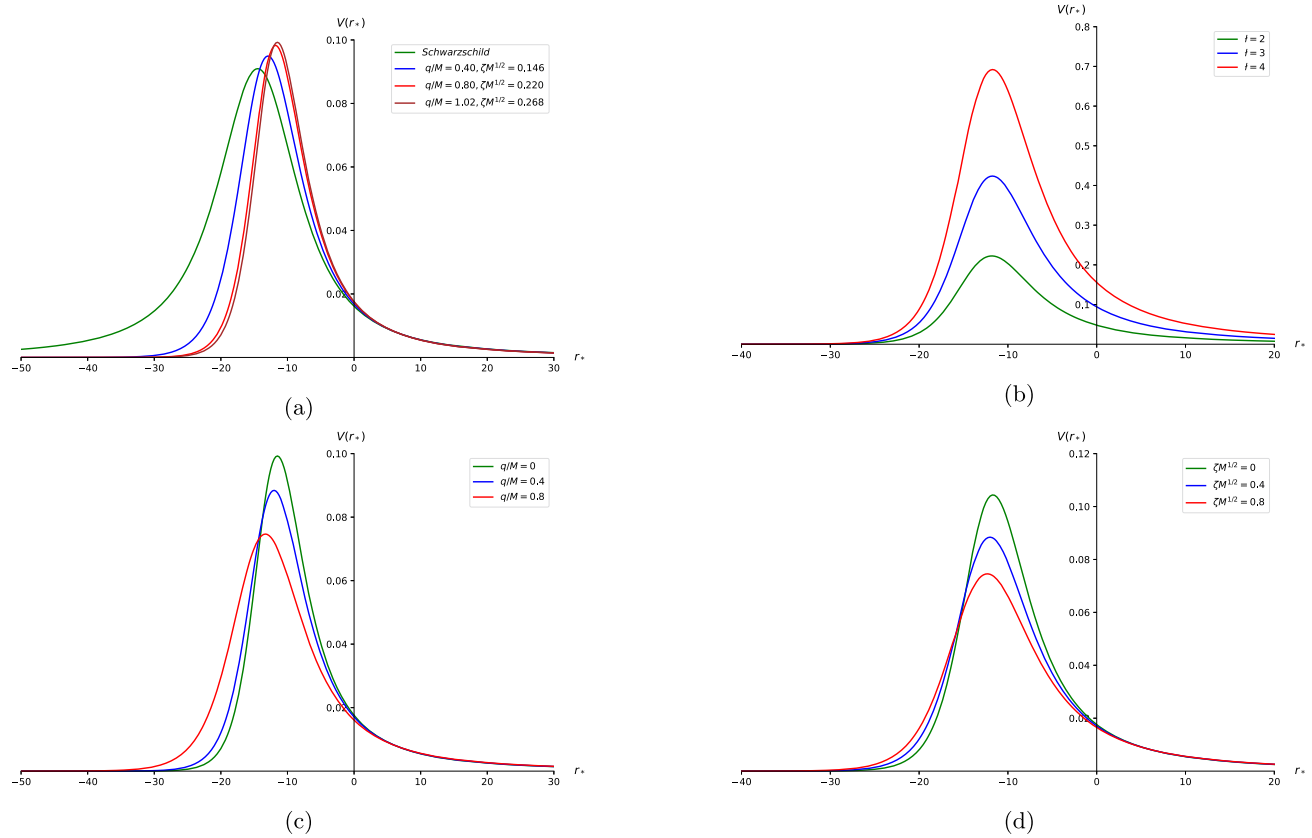

Fig. 3 Variation of the effective potential $V_{\text{eff}}(r)$ for massless scalar field perturbations with the tortoise coordinate r_*. (**a**) Effective potentials for partial parameter combinations when the shadow radius of the NED black hole is fixed to be consistent with that of the Schwarzschild black hole. (**b**) Effective potentials for different angular quantum numbers l with fixed charge q and NED parameter ζ. (**c**) Effective potentials when changing the charge q with fixed NED parameter $\zeta = 0.4$. (**d**) Effective potentials when changing the NED parameter ζ with fixed charge $q = 0.4$. All effective potentials in the figures are plotted with $M = 1$

becomes the dominant factor determining the barrier height when $l > 0$.

In figures (c) and (d), we systematically investigated the independent effects of parameters q and ζ by fixing $\zeta = 0.4$ and $q = 0.4$, respectively. The results consistently show that as either parameter increases, the peak of the effective potential continuously decreases, and the width of the potential barrier increases accordingly.

The height of the potential barrier is mainly positively correlated with the oscillation frequency of QNMs. A lower barrier means gravitational waves can escape more easily, usually corresponding to a lower oscillation frequency. The width of the barrier affects the imaginary part of QNMs. A wider barrier can "trap" the wave for a longer time, thereby extending the damping time (i.e., a smaller absolute value of the imaginary part).

By comparing the morphological changes of these effective potentials, we can more intuitively analyze the QNMs behavior of the black hole.

4 Calculation of quasinormal modes

In this section, we will introduce two different methods for calculating QNMs. QNMs describe the characteristic damped oscillations produced when a black hole relaxes through gravitational wave radiation and other means after being subjected to external perturbations. These modes are characterized by a set of discrete complex frequencies $\omega = \omega_R + i\omega_I$, where the real part ω_R represents the oscillation frequency and the imaginary part ω_I represents the damping rate. For a physically stable system, $\omega_I < 0$. Mathematically, QNMs are the eigen solutions of the wave equation (16) under specific physical boundary conditions. These boundary conditions require the wave to be a purely ingoing wave at the event horizon $r \to r_+$ ($r_* \to -\infty$) and a purely outgoing wave at spatial infinity $r \to \infty$ ($r_* \to +\infty$):

$$\Psi \sim \begin{cases} e^{-i\omega r_*}, & r_* \to -\infty \\ e^{+i\omega r_*}, & r_* \to +\infty \end{cases} \tag{18}$$

To accurately calculate the QNM frequencies of this NED-corrected black hole, this paper adopts two methods for cross-validation: an eigenvalue extraction method based on time-domain evolution and a semi-analytical sixth-order WKB method.

First, this paper uses the time-domain method to directly perform numerical evolution on the original wave Eq. (16). To improve numerical stability, we introduce light-cone coordinates $u = t - r_*$ and $v = t + r_*$, and the wave Eq. (16) is transformed into:

$$4\frac{\partial^2\Psi}{\partial u\partial v} + V_{\text{eff}}(r(u,v))\Psi(u,v) = 0. \tag{19}$$

The method of characteristics integration developed by Gundlach et al. [43] is used for numerical discretization of this equation. Its discrete format has fourth-order accuracy $O(\Delta^4)$ on a uniform (u, v) grid:

$$\Psi_N = \Psi_E + \Psi_W - \Psi_S - \Delta^2 V_{\text{eff}}(r_S)\frac{\Psi_W + \Psi_E}{8} + O(\Delta^4), \tag{20}$$

where N, W, E, S represent the values of Ψ at the four vertices $(u+\Delta, v+\Delta)$, $(u+\Delta, v)$, $(u, v+\Delta)$, (u, v) on the grid, respectively, and Δ is the step size in the u and v directions. A Gaussian wave packet propagating along the v-axis is set, with the form $\Psi(u = 0, v) = A\exp[-(v - v_c)^2/(2\sigma^2)]$, where v_c and σ control the initial position and width of the wave packet, respectively. The evolved time-series signal $\Psi(t, r_{\text{ext}})$ can be extracted at a fixed radial position r_{ext} far from the black hole. A typical time-domain waveform mainly includes three stages: an initial burst dependent on initial conditions, a Ringdown stage determined by the intrinsic properties of the black hole, and a late-time power-law decay tail.

Based on the time-domain evolution shown in Fig. 4, we employ the Prony method to extract the QNM frequencies. The rationale for using this method is straightforward: the Ringdown signal is a superposition of complex exponentials. On a uniform grid, such signals satisfy a linear recurrence relation, meaning any data point can be expressed as a linear combination of its predecessors. The Prony method exploits this linear prediction property to transform the nonlinear frequency fitting problem into a system of linear equations, allowing for efficient parameter extraction. The signal is modeled as [9,44,45]:

$$\Psi(t) \approx \sum_{j=1}^{p} C_j e^{-i\omega_j t}, \tag{21}$$

where $\Psi(t)$ represents the time-series signal during the ringdown phase, and C_j and ω_j denote the complex amplitude and frequency of the jth mode, respectively. The key to accurately extracting QNM frequencies lies in the appropriate selection of the ringdown time window. This window, $[t_{\text{start}}, t_{\text{end}}]$, is determined by standard physical considerations: t_{start} must be chosen sufficiently late to avoid contamination from the initial burst, while t_{end} is set before the signal is overwhelmed by numerical noise. Within this interval, the Prony method is employed to extract the dominant mode frequencies. Further details on the implementation of the method, along with a waveform reconstruction test validating the accuracy of the results (demonstrating a precise match between the fitted and numerical signals), are provided in Appendix A.

To verify the validity of the results, this paper also uses the sixth-order WKB method to calculate QNM frequencies, which has high accuracy when the angular quantum number l is large [46–49]. Its core idea is to correlate the QNM frequency with the properties of the effective potential at its peak. The sixth-order WKB approximation formula is:

$$\frac{i(\omega^2 - V_{\text{max}})}{\sqrt{-2V''_{\text{max}}}} - \sum_{k=2}^{6}\Lambda_k(\omega) = n + \frac{1}{2}, \quad (n = 0, 1, 2, \ldots), \tag{22}$$

where n is the overtone number of the QNM, $V_{\text{max}} \equiv V_{\text{eff}}(r_{0,\text{peak}})$ is the value of the effective potential at its peak, $V''_{\text{max}} \equiv \frac{d^2V_{\text{eff}}}{dr_0^2}\Big|_{r_{0,\text{peak}}}$ is the second derivative of the effective potential with respect to the coordinate r_0 at the peak, and Λ_k represents the kth order correction term [49].

5 Numerical results and analysis of quasinormal modes

This section presents the QNM frequencies calculated using the time-domain Prony method and the sixth-order WKB method, aiming to systematically analyze how the NED parameters (q, ζ) affect the black hole ringdown signal and explore its potential astronomical observation characteristics.

We adopt a double verification strategy to test the accuracy of the calculation methods used. First, to establish the intrinsic accuracy of the sixth-order WKB method, we compare the QNM frequencies of the Schwarzschild black hole calculated by it with the exact values obtained by the Leaver continued fraction method [50], as shown in Table 2. The results show that for the fundamental frequency ($n = 0$) and low-order overtone modes, the accuracy of the WKB method is very high, with relative errors generally lower than 1%, which confirms that it can be used as a reliable benchmark for subsequent comparisons. Second, we use the verified WKB method to cross-validate the accuracy of the

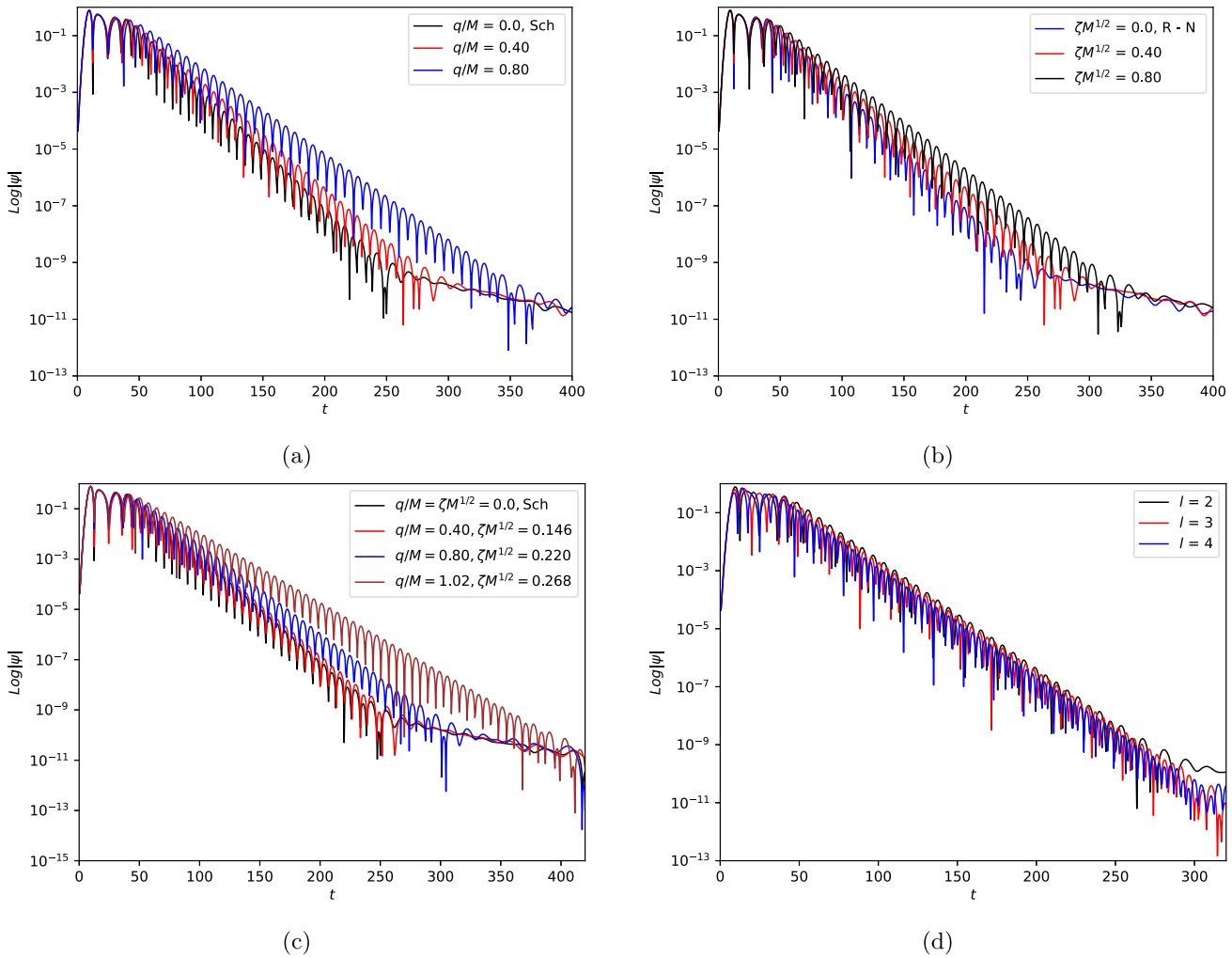

Fig. 4 Time-domain evolution of the absolute value of the scalar field wave function $|\Psi(t)|$. $l = 2$ is set (except for panel (**d**)) and $M = 1$. (**a**) Waveforms for different q with fixed $\zeta = 0.4$. (**b**) Waveforms for different ζ with fixed $q = 0.4$. (**c**) Comparison of waveforms for different parameter combinations under the condition that the shadow radius is fixed to be consistent with that of the Schwarzschild black hole. (**d**) Waveforms for different angular quantum numbers l with fixed $q = 0.4$ and $\zeta = 0.4$

time-domain Prony method in calculating the QNM frequencies of NED black holes. As shown in Table 3, the results of the two methods are in good agreement. The calculated relative errors show that the difference in the real part of the frequency is less than 0.1%, and the difference in the imaginary part is generally within 0.3%. This process fully ensures the reliability of our calculation results.

Subsequently, this paper studies the dependence of QNM frequencies on the NED parameters q and ζ. The calculation results are summarized in Tables 4 and 5, and plotted in Fig. 5. A clear overall trend is that for all (l, n) modes, both the oscillation frequency ω_R and the damping rate $|\omega_I|$ of QNMs decrease monotonically with the increase of q and ζ. This behavior is consistent with the previous analysis of the effective potential: the increase of q and ζ leads to a decrease in the peak value and an increase in the width of the effective potential. The former corresponds to a lower oscillation frequency, and the latter results in a longer damping time (i.e., a smaller $|\omega_I|$) due to the stronger wave "trapping" effect. In addition, the data show that $(n = 0)$ is not only the dominant mode with the slowest decay, but also has a higher oscillation frequency than the corresponding $(n = 1)$. There is also a subtle difference: although ω_R responds approximately linearly to both q and ζ, the behavior of the damping rate $|\omega_I|$ is different. It decreases approximately linearly with ζ, but shows a significant accelerated downward trend with q. This can be attributed to the different embedding methods of the two parameters in the metric (6): ζ is coupled in a linear form, while q contributes nonlinearly to the spacetime geometry through multiple terms such as q^2 and $q^{3/2}$, thereby exerting a nonlinear influence on $|\omega_I|$, which is more sensitive to the barrier structure.

Table 2 QNM frequencies for scalar field perturbations of the Schwarzschild black hole: accuracy comparison between the sixth-order WKB method and the Leaver continued fraction method [50]

(l, n)	ω_{Leaver}	$\omega_{\text{6th WKB}}$	$\Delta_{\omega_R}(\%)$	$\Delta_{\lvert\omega_I\rvert}(\%)$
(0,0)	0.1105–0.1049 i	0.110493–0.100793 i	0.006	3.91
(0,1)	0.0861–0.3481 i	0.089078–0.344344 i	3.46	1.08
(1,0)	0.2929–0.0977 i	0.292910–0.097762 i	0.003	0.063
(1,1)	0.2645–0.3063 i	0.264471–0.306518 i	0.011	0.071
(1,2)	0.2295–0.5401 i	0.231015–0.542164 i	0.660	0.382
(1,3)	0.2033–0.7883 i	0.222096–0.795163 i	9.25	0.871
(2,0)	0.4836–0.0968 i	0.483642–0.096766 i	0.009	0.035
(2,1)	0.4639–0.2956 i	0.463847–0.295627 i	0.011	0.009
(2,2)	0.4305–0.5086 i	0.430386–0.508700 i	0.026	0.020
(2,3)	0.3939–0.7381 i	0.393206–0.739886 i	0.176	0.242

Table 3 Comparison of the fundamental frequency ($n = 0, l = 2$) quasinormal mode frequencies of the scalar field calculated by the sixth-order WKB method and the time-domain Prony method for a series of black hole models with the same shadow radius

(q, ζ)	ω_{WKB}	ω_{Prony}	$\Delta_{\omega_R}(\%)$	$\Delta_{\lvert\omega_I\rvert}(\%)$
Sch (0,0)	0.483642–0.0967661 i	0.483964–0.0965387 i	0.067	0.235
(0.2, 0.102)	0.483648–0.0960251 i	0.483988–0.0958034 i	0.070	0.231
(0.4, 0.146)	0.483671–0.0936885 i	0.483979–0.0934686 i	0.064	0.235
(0.6, 0.183)	0.483696–0.0893215 i	0.483968–0.0891046 i	0.056	0.243
(0.8, 0.220)	0.483497–0.0817084 i	0.483780–0.0814859 i	0.059	0.272
(1.02, 0.268)	0.481800–0.0639091 i	0.482087–0.0638081 i	0.060	0.158

Table 4 Variation of QNM frequencies with ζ for a fixed charge $q = 0.4$

(l, n)	$\zeta = 0.0$	$\zeta = 0.2$	$\zeta = 0.4$	$\zeta = 0.6$	$\zeta = 0.8$
(0, 0)	0.113891–0.101455 i	0.109010–0.095923 i	0.104396–0.090573 i	0.099916–0.085525 i	0.095562–0.080785 i
(1, 0)	0.301325–0.098512 i	0.289853–0.093140 i	0.278611–0.088039 i	0.267622–0.083206 i	0.256904–0.078638 i
(2, 0)	0.497411–0.097561 i	0.478636–0.092291 i	0.460222–0.087281 i	0.442206–0.082528 i	0.424620–0.078032 i
(0, 1)	0.092900–0.344517 i	0.088899–0.325589 i	0.085296–0.306760 i	0.081816–0.289034 i	0.078429–0.272488 i
(1, 1)	0.273842–0.308243 i	0.264479–0.290996 i	0.255200–0.274662 i	0.246022–0.259233 i	0.236969–0.244693 i
(2, 1)	0.478295–0.297811 i	0.461054–0.281536 i	0.444053–0.266082 i	0.427332–0.251445 i	0.410932–0.237615 i

Table 5 Variation of QNM frequencies with charge q for a fixed $\zeta = 0.4$

(l, n)	$q = 0.0$	$q = 0.2$	$q = 0.4$	$q = 0.6$	$q = 0.8$
(0, 0)	0.110493–0.100793 i	0.108030–0.097071 i	0.104396–0.090574 i	0.100397–0.082502 i	0.096243–0.072534 i
(1, 0)	0.292910–0.097762 i	0.287097–0.094208 i	0.278611–0.088039 i	0.269466–0.080250 i	0.260357–0.070782 i
(2, 0)	0.483642–0.096766 i	0.474120–0.093299 i	0.460222–0.087281 i	0.445290–0.079666 i	0.430589–0.070390 i
(0, 1)	0.089078–0.344344 i	0.087359–0.330852 i	0.085296–0.306760 i	0.083829–0.275964 i	0.080595–0.239032 i
(1, 1)	0.264471–0.306518 i	0.260403–0.294909 i	0.255200–0.274662 i	0.250253–0.249134 i	0.245679–0.218181 i
(2, 1)	0.463847–0.295627 i	0.455591–0.284840 i	0.444053–0.266082 i	0.432106–0.242363 i	0.420643–0.213512 i

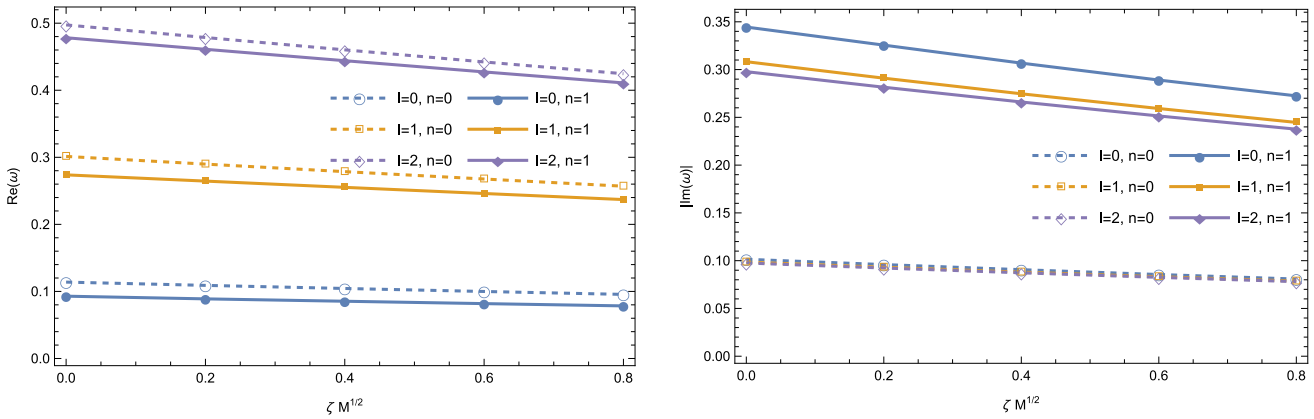

(a) Fixed $q = 0.4$

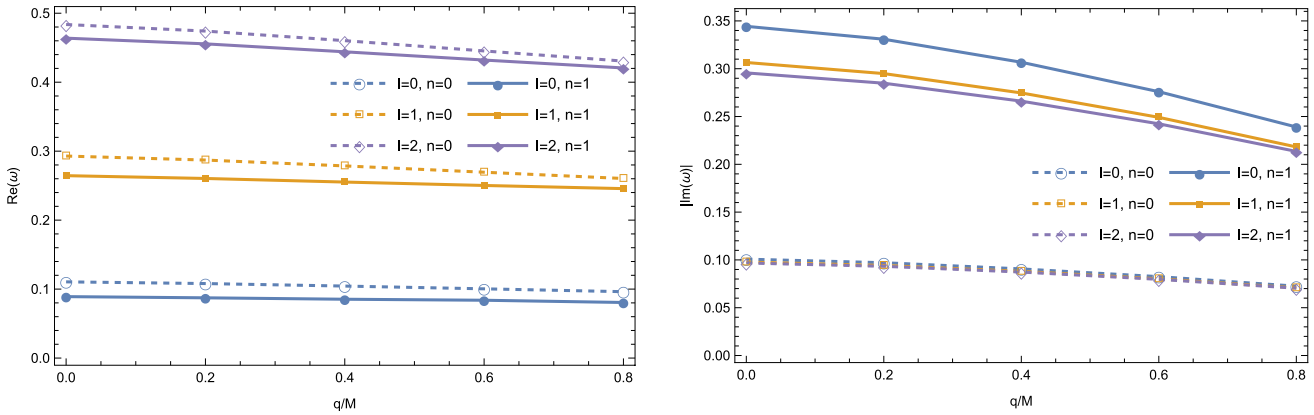

(b) Fixed $\zeta = 0.4$

Fig. 5 Dependence of QNM frequencies on the parameters of the NED-corrected black hole. The figure shows the results of the fundamental frequency mode ($n = 0$) and the first overtone mode ($n = 1$) for different angular quantum numbers l. (**a**) Variation of ω with ζ; (**b**) Variation of ω with q

Finally, it is worth noting: Can QNMs break the model degeneracy existing in black hole shadow observations? To this end, we calculated the QNM frequencies of a series of NED-corrected black hole "degenerates" that have exactly the same shadow radius as the Schwarzschild black hole. Based on the data in Table 3, Fig. 6 is plotted, which reveals a striking duality. On the one hand, the oscillation frequency ω_R exhibits remarkable stability, with extremely small deviations from the Schwarzschild reference value over a wide parameter range. A tiny maximum value only appears near $(q = 0.6, \zeta = 0.183)$, and then decreases significantly when approaching the extremal black hole. On the other hand, the damping rate $|\omega_I|$ is extremely sensitive to parameter changes, showing a strictly monotonic decreasing trend with the increase of (q, ζ), which systematically deviates from the Schwarzschild reference value. The root cause of this behavioral difference is that the "same-shadow" constraint mainly fixes the behavior of the effective potential near the photon sphere, thereby stabilizing ω_R, which is mainly determined by the barrier height; however, this constraint does not limit the change of the barrier width, which determines the damping rate $|\omega_I|$. Therefore, these results strongly prove that although the electromagnetic observation characteristics (shadows) of different black hole models may be degenerate, their gravitational wave signals (QNMs) can be clearly distinguished. In particular, the imaginary part of QNMs can be used as a more sensitive probe for us to detect the spacetime geometry of black holes.

6 Greybody factors

The spacetime curvature around a black hole forms an effective gravitational potential barrier that filters particles emitted near the horizon, thereby altering their final observable radiation spectrum. This process can be described by

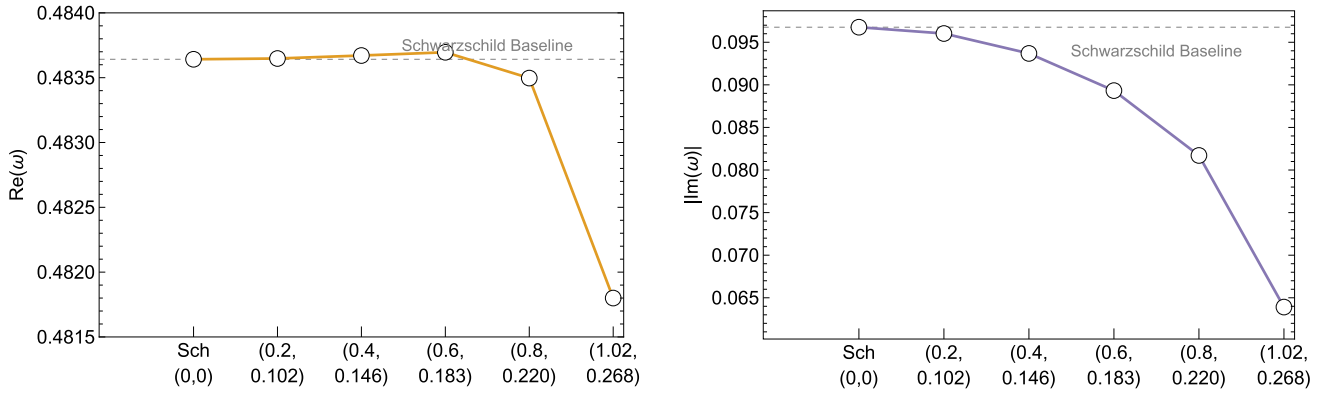

Fig. 6 Comparison of the fundamental frequency ($l = 2, n = 0$) QNM frequencies between the Schwarzschild black hole and its "same-shadow" NED-corrected black hole degenerate models. Left panel: real part of the frequency (ω_R). Right panel: absolute value of the imaginary part of the frequency ($|\omega_I|$). A series of parameter combinations (q, ζ) satisfying the "same-shadow" condition are listed on the abscissa, and their values are consistent with Table 3. The dashed line in the figure represents the reference value of the Schwarzschild black hole

a standard scattering problem, where a plane wave incident from infinity is partially reflected by the barrier and partially transmitted into the black hole horizon. The transmission probability in this process is the frequency-dependent greybody factor $\Gamma(\omega)$. According to particle number conservation, its relationship with the reflection probability $|\mathcal{R}(\omega)|^2$ is $\Gamma(\omega) = 1 - |\mathcal{R}(\omega)|^2$.

The use of the WKB approximation method to calculate the reflection coefficient $\mathcal{R}(\omega)$ and transmission coefficient is not new; it has been applied in various scenarios for calculations [47,49,51–53]. Within this framework, the reflection coefficient around a black hole is given by [46]:

$$\mathcal{R}(\omega) = (1 + e^{-2\pi i\alpha})^{-\frac{1}{2}}, \tag{23}$$

where the expression for the phase factor α is given by [54]:

$$\alpha = \frac{i(\omega^2 - V_{\text{peak}})}{\sqrt{-2V''_{\text{peak}}}} - \sum_{k=2}^{6} \Lambda_k. \tag{24}$$

By calculating α, we can obtain the reflection probability $|\mathcal{R}(\omega)|^2$, and then determine the greybody factor $\Gamma(\omega)$.

Figure 7 shows the variation of the greybody factor with frequency and NED parameters for a fixed angular quantum number $l = 2$. An obvious overall trend can be observed from Fig. 7a and b: increasing either q or ζ shifts the entire greybody factor curve to the left. This indicates that for a scalar particle with a fixed frequency ω, its escape probability increases as q or ζ increases. This phenomenon is consistent with the discussion on the effective potential barrier V_{eff}: the increase of q or ζ lowers the peak of the barrier, making it easier for low-energy particles to penetrate, thereby increasing the transmission rate $\Gamma(\omega)$. When the frequency is sufficiently high, all curves quickly approach 1, because high-energy particles can easily cross the barrier, and their behavior is dominated by geometric optics, which is no longer sensitive to the specific structure of the barrier.

In addition, the analysis of "degenerate models" of black holes with the same black hole shadow (Fig. 7c) shows that their transmission behavior exhibits a complex frequency-dependent characteristic. There exists a crossing point at $\omega \approx 0.47$. Before the crossing point (low-frequency region), the greybody factor of the Schwarzschild black hole (blue line) is the highest, while the NED black hole with larger parameters (q, ζ) has a lower greybody factor. However, after the crossing point, the greybody factor curve of the NED black hole rapidly surpasses that of the Schwarzschild black hole due to its extremely steep transmission rate, and the larger the parameters, the steeper the slope. This crossing phenomenon reveals a profound physical scenario: to maintain the same shadow, although the effective potential barrier of the NED black hole has a lower peak, its base is wider. In the low-frequency region, particles mainly pass through quantum tunneling, and the wider barrier base inhibits the transmission rate; in the high-frequency region, the particle energy is sufficient to cross the barrier, and at this time, the lower barrier peak dominates the behavior, leading to a sharp increase in the transmission rate.

7 Conclusion

This paper studies an NED black hole model with logarithmic correction terms, aiming to explore a core issue in astrophysical observations: whether models degenerate in electromagnetic observations (i.e., having the same shadow radius) can be effectively distinguished through gravitational wave and quantum radiation characteristics. To establish the connection between this model and astrophysical observations,

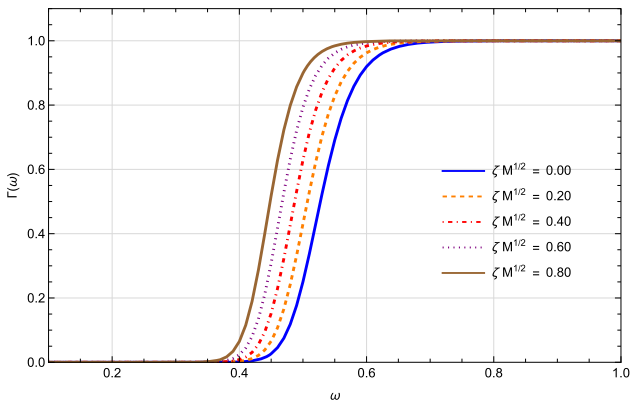

(a) Variation of the greybody factor with ζ

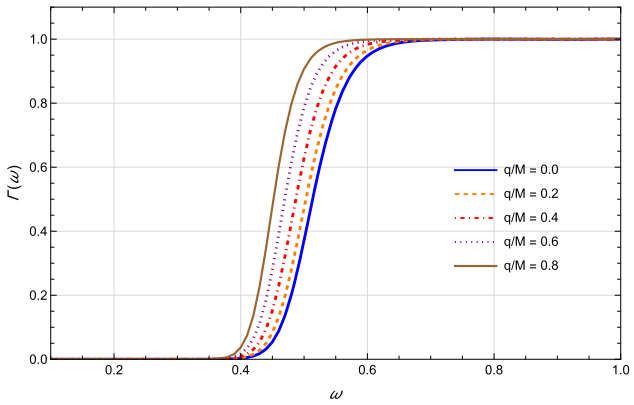

(b) Variation of the greybody factor with q

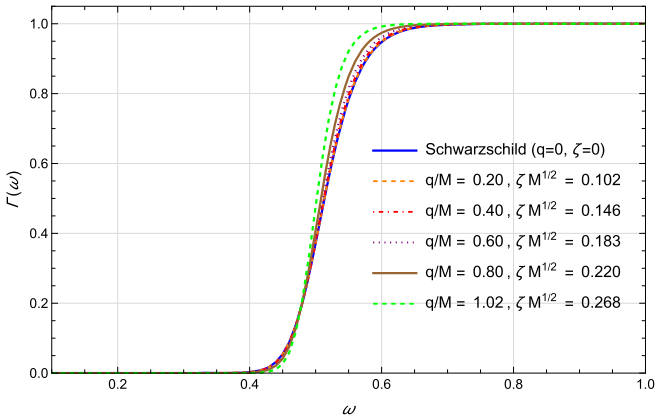

(c) Greybody factors of "degenerate" black holes with the same shadow as the Schwarzschild black hole

Fig. 7 Variation of the greybody factor $\Gamma(\omega)$ of the scalar field ($l = 2$) with frequency ω. (**a**) Fixed $q = 0.4$, varying ζ. (**b**) Fixed $\zeta = 0.4$, varying q. (**c**) Comparison between the Schwarzschild black hole and a series of NED black hole models with the same shadow radius

we use the shadow observation data of M87* from the EHT to impose constraints on the parameter space (q, ζ) of the model.

The analysis of the black hole's QNMs shows that the model parameters q and ζ affect the QNM spectrum in different ways. Specifically, when either parameter is fixed, both the oscillation frequency and the damping rate decrease linearly with ζ or q; when ζ increases, the damping rate also decreases linearly, but it shows a stronger nonlinear dependence on q with a more significant downward trend. Compared with the standard Schwarzschild black hole ($q = 0$), this NED-corrected black hole has a lower oscillation frequency and a longer damping time. Meanwhile, for those "degenerate" models that have the same shadow as the Schwarzschild black hole, although the differences in their oscillation frequencies are extremely small and almost indistinguishable, their damping rates exhibit high sensitivity and monotonic dependence on the NED parameters. This core result clearly indicates that the damping time of QNMs, rather than the oscillation frequency, is the primary physical quantity for revealing the characteristics of such non-standard black holes and breaking observational degeneracy.

The analysis of the greybody factor not only can be mutually confirmed with the variation trends of the effective potential and QNMs, but also provides a second independent and powerful way to distinguish degenerate models. Whether changing the parameter q or ζ, the effective potential barrier of the model is systematically changed, leading to an overall shift of the peak of its Hawking radiation spectrum to the low-frequency region. Compared with the Schwarzschild black hole, the Hawking radiation spectrum of the NED black hole with the same shadow is significantly reshaped: it is suppressed at extremely low frequencies but sharply enhanced within a specific frequency window. This indicates that the peak position and overall shape of the observed Hawking radiation spectrum will change. This unique spectral feature provides a highly promising window for distinguishing different black hole models and testing nonlinear electrodynamics theories through high-precision astronomical observation methods (such as detecting Hawking radiation) in the future. More importantly, it indirectly provides a refined probe for

"tomography" of the effective potential barrier structure, thereby breaking the degeneracy of electromagnetic observations.

In summary, even if future electromagnetic observations of black hole shadows are completely consistent with the predictions of general relativity, gravitational wave signals (especially their damping characteristics) and Hawking radiation spectra are still powerful tools for breaking model degeneracy. These unique signal characteristics provide a feasible way to test alternative gravitational theories and explore new physics through future multi-messenger astronomy observations.

Acknowledgements This research was supported by the National Natural Science Foundation of China (Grant No. 12265007) and the Guizhou Provincial Major Scientific and Technological Program (Grant No. XKBF (2025)010).

Data Availability Statement This manuscript has no associated data. [Authors' comment: Data sharing not applicable to this article as no datasets were generated or analysed during the current study.].

Code Availability Statement This manuscript has no associated code/software. [Authors' comment: Code/Software sharing not applicable to this article as no code/software was generated or analysed during the current study.].

Open Access This article is licensed under a Creative Commons Attribution 4.0 International License, which permits use, sharing, adaptation, distribution and reproduction in any medium or format, as long as you give appropriate credit to the original author(s) and the source, provide a link to the Creative Commons licence, and indicate if changes were made. The images or other third party material in this article are included in the article's Creative Commons licence, unless indicated otherwise in a credit line to the material. If material is not included in the article's Creative Commons licence and your intended use is not permitted by statutory regulation or exceeds the permitted use, you will need to obtain permission directly from the copyright holder. To view a copy of this licence, visit http://creativecommons.org/licenses/by/4.0/.
Funded by SCOAP[3].

Appendix A: Prony method

In this paper, we adopt a standard technique in the field of signal processing – the Prony method-to extract the frequencies of QNMs from time-domain waveform data. The basic assumption of this method is that the QNM can be accurately modeled as a superposition of p damped complex exponential functions:

$$\Psi(t) \approx \sum_{j=1}^{p} C_j e^{-i\omega_j t} \tag{A1}$$

where C_j are complex amplitudes, and ω_j are complex frequencies whose imaginary parts represent the damping rates of the modes.

For a discrete time-domain signal $x_n = \Psi(nh)$ sampled at a uniform time interval h, the model can be converted into the following discrete form:

$$x_n = \sum_{j=1}^{p} C_j z_j^n, \quad \text{where} \quad z_j = e^{-i\omega_j h}. \tag{A2}$$

The core idea of the Prony method is to determine the frequency information by solving the roots z_j of a characteristic polynomial $A(z) = \sum_{k=0}^{p} a_k z^{p-k}$. The coefficients a_k of this polynomial (with the convention $a_0 = 1$) can be determined by solving the following linear system of equations:

$$\begin{pmatrix} x_{p-1} & x_{p-2} & \cdots & x_0 \\ x_p & x_{p-1} & \cdots & x_1 \\ \vdots & \vdots & \ddots & \vdots \\ x_{N-1} & x_{N-2} & \cdots & x_{N-p} \end{pmatrix} \begin{pmatrix} a_1 \\ a_2 \\ \vdots \\ a_p \end{pmatrix} = - \begin{pmatrix} x_p \\ x_{p+1} \\ \vdots \\ x_N \end{pmatrix} \tag{A3}$$

This matrix equation, denoted as $Xa = -x$, is usually overdetermined, so the coefficient vector a can be solved by the least squares method:

$$a = -(X^+ X)^{-1} X^+ x, \tag{A4}$$

where X^+ is the Hermitian conjugate of matrix X.

Once the polynomial coefficients a_k are obtained, all roots z_j of the polynomial $A(z)$ can be found by numerical methods. Finally, the complex frequencies ω_j of the QNMs can be extracted from these roots through the following relationship:

$$\omega_j = \frac{i}{h} \ln(z_j). \tag{A5}$$

To validate the robustness and accuracy of the Prony method across the entire parameter space, we performed waveform reconstruction tests for three representative cases corresponding to the scenarios analyzed in Fig. 4:

(i) The general NED black hole case ($q/M = 0.4$, $\zeta M^{1/2} = 0.4$);
(ii) The Reissner–Nordström (R–N) limit ($q/M = 0.4$, $\zeta M^{1/2} = 0$); and
(iii) The highly charged degenerate black hole case ($q/M = 0.80$, $\zeta M^{1/2} = 0.220$).

Using the fundamental frequencies ω_0 extracted in Tables 3 and 5, we reconstructed the time-domain signals using the ansatz $\Psi_{\rm rec}(t) \approx {\rm Re}[Ce^{-i\omega_0 t}]$ [55]. While the frequency ω_0 is fixed by the extraction algorithm, the complex amplitude C (determined by the initial excitation) was obtained via a least-squares fit to the numerical data within the ringdown window (typically chosen as $75 \leq t \leq 195$). As illustrated

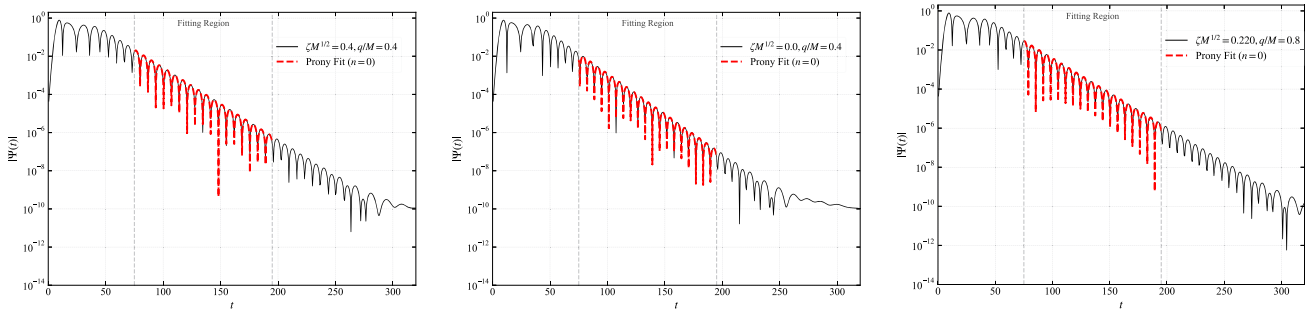

(a) $\zeta M^{1/2} = 0.4, q/M = 0.4$ (b) $\zeta M^{1/2} = 0, q/M = 0.4$ (c) $\zeta M^{1/2} = 0.220, q/M = 0.80$

Fig. 8 Validation of extracted QNM frequencies via waveform reconstruction. The figure compares the numerical simulation waveforms (black solid lines) with the reconstructed waveforms based on Prony-extracted frequencies (red dashed lines) for three representative physical scenarios: (**a**) general NED black hole; (**b**) R-N black hole limit; (**c**) degenerate black hole model. In all panels, the curves overlap perfectly within the fitting interval indicated by gray dashed lines ($75 \leq t \leq 195$), verifying the accuracy of the frequency extraction

in Fig. 8, the reconstructed waveforms (red dashed lines) exhibit excellent agreement with the numerical simulations (black solid lines) in all panels. This precise alignment of both the oscillation phase and the damping envelope confirms that the extracted QNM frequencies accurately characterize the dynamical response of the scalar field.

References

1. S.H. Mazharimousavi, Phys. Lett. B **841**, 137948 (2023). https://doi.org/10.1016/j.physletb.2023.137948. arXiv:2305.01048 [gr-qc]
2. B.P. Abbott et al. (LIGO Scientific, Virgo), Phys. Rev. Lett. **116**, 061102 (2016). https://doi.org/10.1103/PhysRevLett.116.061102. arXiv:1602.03837 [gr-qc]
3. B.P. Abbott et al. (LIGO Scientific, Virgo), Phys. Rev. Lett. **116**, 241103 (2016). https://doi.org/10.1103/PhysRevLett.116.241103. arXiv:1606.04855 [gr-qc]
4. B.P. Abbott et al. (LIGO Scientific, Virgo), Phys. Rev. Lett. **119**, 161101 (2017). https://doi.org/10.1103/PhysRevLett.119.161101. arXiv:1710.05832 [gr-qc]
5. R. Abbott et al. (KAGRA, VIRGO, LIGO Scientific), Astrophys. J. Suppl. **267**, 29 (2023). https://doi.org/10.3847/1538-4365/acdc9f. arXiv:2302.03676 [gr-qc]
6. K. Akiyama et al. (Event Horizon Telescope), Astrophys. J. Lett. **875**, L1 (2019). https://doi.org/10.3847/2041-8213/ab0ec7. arXiv:1906.11238 [astro-ph.GA]
7. R. Abbott et al. (LIGO Scientific, KAGRA, VIRGO), Astrophys. J. Lett. **915**, L5 (2021). https://doi.org/10.3847/2041-8213/ac082e. arXiv:2106.15163 [astro-ph.HE]
8. R. Abbott et al. (LIGO Scientific, Virgo), Phys. Rev. D **102**, 043015 (2020). https://doi.org/10.1103/PhysRevD.102.043015. arXiv:2004.08342 [astro-ph.HE]
9. R.A. Konoplya, A. Zhidenko, Rev. Mod. Phys. **83**, 793 (2011). https://doi.org/10.1103/RevModPhys.83.793. arXiv:1102.4014 [gr-qc]
10. K.D. Kokkotas, B.G. Schmidt, Living Rev. Relativ. **2**, 2 (1999). https://doi.org/10.12942/lrr-1999-2. arXiv:gr-qc/9909058
11. E. Berti, V. Cardoso, A.O. Starinets, Class. Quantum Gravity **26**, 163001 (2009). https://doi.org/10.1088/0264-9381/26/16/163001. arXiv:0905.2975 [gr-qc]
12. S.V. Bolokhov, M. Skvortsova, (2025). arXiv:2504.05014 [gr-qc]
13. V. Cardoso, E. Franzin, P. Pani, Phys. Rev. Lett. **116**, 171101 (2016). [Erratum: Phys. Rev. Lett. **117**, 089902 (2016)]. https://doi.org/10.1103/PhysRevLett.116.171101. arXiv:1602.07309 [gr-qc]
14. H. Gong, S. Li, D. Zhang, G. Fu, J.-P. Wu, Phys. Rev. D **110**, 044040 (2024). https://doi.org/10.1103/PhysRevD.110.044040. arXiv:2312.17639 [gr-qc]
15. R.G. Daghigh, M.D. Green, G. Kunstatter, Phys. Rev. D **103**, 084031 (2021). https://doi.org/10.1103/PhysRevD.103.084031. arXiv:2012.13359 [gr-qc]
16. Z.S. Moreira, H.C.D. Lima, L.C.B. Crispino, C.A.R. Herdeiro, Phys. Rev. D **107**, 104016 (2023). https://doi.org/10.1103/PhysRevD.107.104016. arXiv:2302.14722 [gr-qc]
17. S.V. Bolokhov, Phys. Rev. D **109**, 064017 (2024). https://doi.org/10.1103/PhysRevD.109.064017
18. R.A. Konoplya, Z. Stuchlik, A. Zhidenko, A.F. Zinhailo, Phys. Rev. D **107**, 104050 (2023). https://doi.org/10.1103/PhysRevD.107.104050. arXiv:2303.01987 [gr-qc]
19. R.A. Konoplya, A. Zhidenko, JCAP **09**, 068 (2024). https://doi.org/10.1088/1475-7516/2024/09/068. arXiv:2406.11694 [gr-qc]
20. R.A. Konoplya, A. Zhidenko, Phys. Lett. B **861**, 139288 (2025). https://doi.org/10.1016/j.physletb.2025.139288. arXiv:2408.11162 [gr-qc]
21. S.V. Bolokhov, M. Skvortsova, JCAP **04**, 025 (2025). https://doi.org/10.1088/1475-7516/2025/04/025. arXiv:2412.11166 [gr-qc]
22. N. Oshita, JCAP **04**, 013 (2023). https://doi.org/10.1088/1475-7516/2023/04/013. arXiv:2208.02923 [gr-qc]
23. N. Oshita, Phys. Rev. D **109**, 104028 (2024). https://doi.org/10.1103/PhysRevD.109.104028. arXiv:2309.05725 [gr-qc]
24. D. N. , Phys. Rev. D **13**, 198 (1976)
25. D. N. , Phys. Rev. D **14**, 3260 (1976). https://doi.org/10.1103/PhysRevD.14.3260
26. P. Kanti, Int. J. Mod. Phys. A **19**, 4899 (2004). https://doi.org/10.1142/S0217751X04018324. arXiv:hep-ph/0402168
27. M. Born, L. Infeld, Proc. R. Soc. Lond. A **144**, 425 (1934). https://doi.org/10.1098/rspa.1934.0059
28. E. Ayon-Beato, A. Garcia, Phys. Lett. B **493**, 149 (2000). https://doi.org/10.1016/S0370-2693(00)01125-4. arXiv:gr-qc/0009077
29. Z.-Y. Fan, X. Wang, Phys. Rev. D **94**, 124027 (2016). https://doi.org/10.1103/PhysRevD.94.124027. arXiv:1610.02636 [gr-qc]
30. M.E. Rodrigues, E.L.B.G.T. Marques, V.T. Zanchin, Phys. Rev. D **94**, 024062 (2016). [Addendum: Phys. Rev. D **94**, 049904 (2016)].

https://doi.org/10.1103/PhysRevD.94.024062. arXiv:1511.00569 [gr-qc]
31. K.A. Bronnikov, Int. J. Mod. Phys. D **27**, 1841005 (2018). https://doi.org/10.1142/S0218271818410055. arXiv:1711.00087 [gr-qc]
32. A. Burinskii, S.R. Hildebrandt, Phys. Rev. D **65**, 104017 (2002). https://doi.org/10.1103/PhysRevD.65.104017. arXiv:hep-th/0202066
33. R. Kumar, A. Kumar, S.G. Ghosh, Astrophys. J. **896**, 89 (2020). https://doi.org/10.3847/1538-4357/ab8c4a. arXiv:2006.09869 [gr-qc]
34. F. Atamurotov, S. Shaymatov, P. Sheoran, S. Siwach, JCAP **08**, 045 (2021). https://doi.org/10.1088/1475-7516/2021/08/045. arXiv:2105.02214 [gr-qc]
35. E. Sucu, A. Övgün, Phys. Dark Univ. **44**, 101446 (2024). https://doi.org/10.1016/j.dark.2024.101446. arXiv:2403.07044 [gr-qc]
36. S. Shaymatov, B. Ahmedov, M. De Laurentis, M. Jamil, Q. Wu, A. Wang, M. Azreg-Aïnou, Astrophys. J. **959**, 6 (2023). https://doi.org/10.3847/1538-4357/acfcba. arXiv:2307.10804 [gr-qc]
37. R. Kumar Walia, Phys. Rev. D **110**, 064058 (2024). https://doi.org/10.1103/PhysRevD.110.064058. arXiv:2409.13290 [gr-qc]
38. H. Rehman, G. Abbas, T. Zhu, Q. Wu, G. Mustafa, Eur. Phys. J. C **84**, 988 (2024). https://doi.org/10.1140/epjc/s10052-024-13384-3
39. H. Waseem, N.J.L.S. Lobos, A. Övgün, R.C. Pantig, (2025). arXiv:2502.04044 [gr-qc]
40. D. Psaltis et al. (Event Horizon Telescope), Phys. Rev. Lett. **125**, 141104 (2020). https://doi.org/10.1103/PhysRevLett.125.141104. arXiv:2010.01055 [gr-qc]
41. O.Y. Tsupko, Z. Fan, G.S. Bisnovatyi-Kogan, Class. Quantum Gravity **37**, 065016 (2020). https://doi.org/10.1088/1361-6382/ab6f7d. arXiv:1905.10509 [gr-qc]
42. V.I. Dokuchaev, N.O. Nazarova, Usp. Fiz. Nauk **190**, 627 (2020). https://doi.org/10.3367/UFNe.2020.01.038717. arXiv:1911.07695 [gr-qc]
43. C. Gundlach, R.H. Price, J. Pullin, Phys. Rev. D **49**, 883 (1994). https://doi.org/10.1103/PhysRevD.49.883. arXiv:gr-qc/9307009
44. A. Chowdhury, N. Banerjee, Phys. Rev. D **102**, 124051 (2020). https://doi.org/10.1103/PhysRevD.102.124051. arXiv:2006.16522 [gr-qc]
45. E. Berti, V. Cardoso, J.A. Gonzalez, U. Sperhake, Phys. Rev. D **75**, 124017 (2007). https://doi.org/10.1103/PhysRevD.75.124017. arXiv:gr-qc/0701086
46. B.F. Schutz, C.M. Will, Astrophys. J. Lett. **291**, L33 (1985). https://doi.org/10.1086/184453
47. S. Iyer, C.M. Will, Phys. Rev. D **35**, 3621 (1987). https://doi.org/10.1103/PhysRevD.35.3621
48. S. Iyer, Phys. Rev. D **35**, 3632 (1987). https://doi.org/10.1103/PhysRevD.35.3632
49. R.A. Konoplya, Phys. Rev. D **68**, 024018 (2003). https://doi.org/10.1103/PhysRevD.68.024018. arXiv:gr-qc/0303052
50. E. Seidel, S. Iyer, Phys. Rev. D **41**, 374 (1990). https://doi.org/10.1103/PhysRevD.41.374
51. J. Grain, A. Barrau, Nucl. Phys. B **742**, 253 (2006). https://doi.org/10.1016/j.nuclphysb.2006.03.001. arXiv:hep-th/0603042
52. B. Toshmatov, Z. Stuchlík, J. Schee, B. Ahmedov, Phys. Rev. D **93**, 124017 (2016). https://doi.org/10.1103/PhysRevD.93.124017. arXiv:1605.02058 [gr-qc]
53. R.A. Konoplya, A. Zhidenko, Phys. Rev. D **81**, 124036 (2010). https://doi.org/10.1103/PhysRevD.81.124036. arXiv:1004.1284 [hep-th]
54. R.A. Konoplya, A. Zhidenko, A.F. Zinhailo, Class. Quantum Gravity **36**, 155002 (2019). https://doi.org/10.1088/1361-6382/ab2e25. arXiv:1904.10333 [gr-qc]
55. M. Giesler, M. Isi, M.A. Scheel, S. Teukolsky, Phys. Rev. X **9**, 041060 (2019). https://doi.org/10.1103/PhysRevX.9.041060. arXiv:1903.08284 [gr-qc]